Supporting Information for

# Lanthanide-based Metal–Organic Frameworks Containing "V-Shaped" Tetracarboxylate Ligands: Synthesis, Crystal Structures, "Naked-Eye" Luminescent Detection and Catalytic Properties

Pengyan Wu,[†] Lingling Xia,[†] Mengjie Huangfu,[†] Fubin Fu,[†] Mengqiu Wang,[†] Bingxin Wen,[†] Ziyun Yang[†] and Jian Wang*,[†]

[†] School of Chemistry and Materials Science & Jiangsu Key Laboratory of Green Synthetic Chemistry for Functional Materials, Jiangsu Normal University, Xuzhou, Jiangsu, 221116, People's Republic of China.

**Figure S1** The chemical structure of 5,5'-methylenediisophthalic acid ($H_4$MDIA).

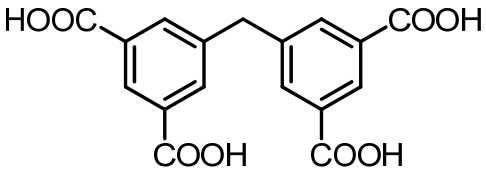


**Figure S2** The asymmetric unit of Tb−**MDIA**, Tb = cyan, O = red, C = gray and H = white.

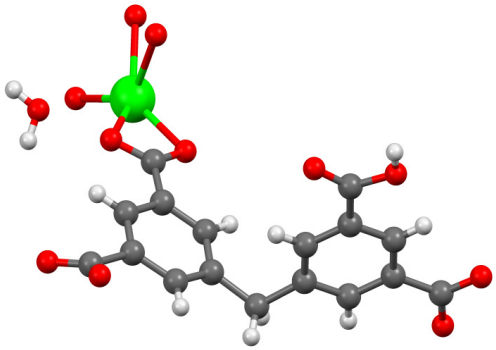

**Figure S3** The coordination mode of H**MDIA**$^{3-}$ ligands in Tb−**MDIA**, Tb = cyan, O = red, C = gray and H = white.

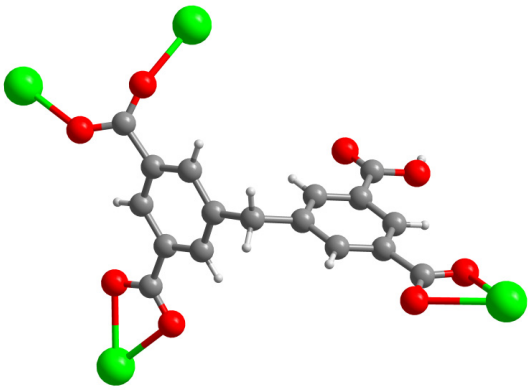

**Figure S4** The asymmetric unit of Ho−**MDIA**, Ho = cyan, O = red, C = gray and H = white.

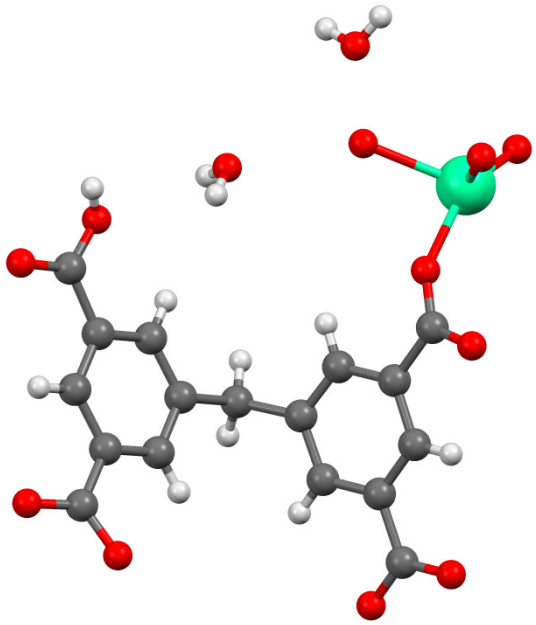

**Figure S5** The coordination mode of H**MDIA**$^{3-}$ ligands in Ho−**MDIA**, Ho = cyan, O = red, C = gray and H = white.

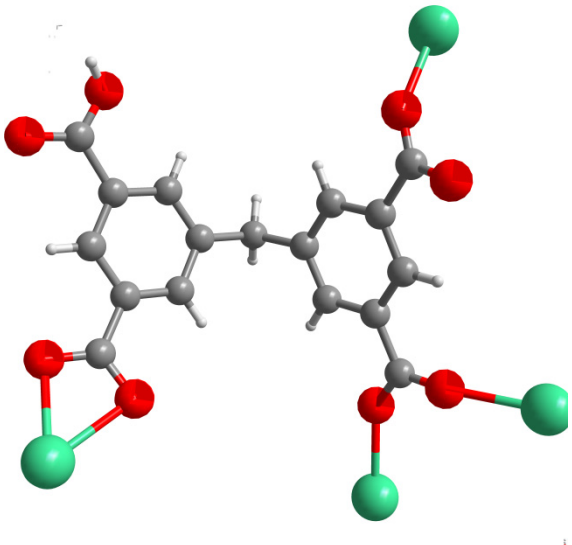

**Figure S6** The asymmetric unit of Nd−**MDIA**, Nd = cyan, O = red, C = gray and H = white.

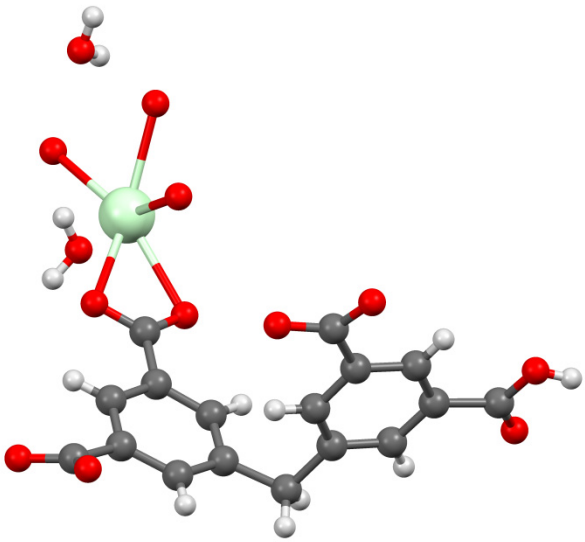

**Figure S7** The coordination mode of H**MDIA**$^{3-}$ ligands in Nd−**MDIA**, Nd = cyan, O = red, C = gray and H = white.

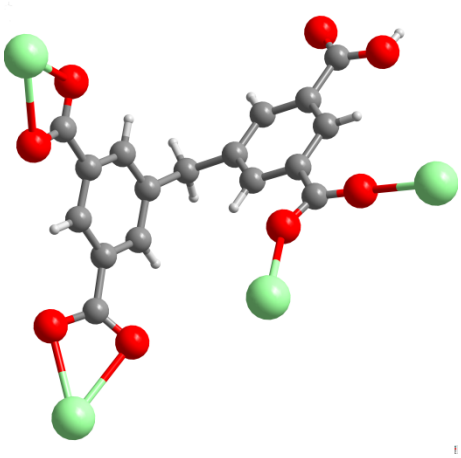

**Table S1** Selective bond distance (Å) and angle (°) in Tb−**MDIA.**

| | | | |
|---|---|---|---|
| Tb(1)-O(3A) | 2.317(3) | Tb(1)-O(4B) | 2.366(3) |
| Tb(1)-O(1) | 2.407(3) | Tb(1)-O(6C) | 2.413(3) |
| Tb(1)-O(2W) | 2.453(3) | Tb(1)-O(3W) | 2.455(3) |
| Tb(1)-O(1W) | 2.490(3) | Tb(1)-O(2) | 2.498(3) |
| Tb(1)-O(5C) | 2.563(3) | | |
| O(3A)-Tb(1)-O(4B) | 95.29(11) | O(3A)-Tb(1)-O(1) | 79.39(12) |
| O(4B)-Tb(1)-O(1) | 125.01(11) | O(3A)-Tb(1)-O(6C) | 77.74(11) |
| O(4B)-Tb(1)-O(6C) | 146.80(11) | O(1)-Tb(1)-O(6C) | 86.04(11) |
| O(3A)-Tb(1)-O(2W) | 134.62(11) | O(4B)-Tb(1)-O(2W) | 80.95(11) |
| O(1)-Tb(1)-O(2W) | 138.74(11) | O(6C)-Tb(1)-O(2W) | 81.44(11) |
| O(3A)-Tb(1)-O(3W) | 148.94(12) | O(4B)-Tb(1)-O(3W) | 77.59(11) |
| O(1)-Tb(1)-O(3W) | 80.32(12) | O(6C)-Tb(1)-O(3W) | 123.91(11) |
| O(2W)-Tb(1)-O(3W) | 74.73(12) | O(3A)-Tb(1)-O1(W) | 67.63(11) |
| O(4B)-Tb(1)-O(1W) | 70.73(11) | O(1)-Tb(1)-O(1W) | 145.21(11) |
| O(6C)-Tb(1)-O(1W) | 76.69(10) | O(2W)-Tb(1)-O(1W) | 68.54(11) |
| O(3W)-Tb(1)-O(1W) | 134.29(11) | O(3A)-Tb(1)-O(2) | 73.98(11) |
| O(4B)-Tb(1)-O(2) | 72.69(11) | O(1) -Tb(1)-O(2) | 53.07(10) |
| O(6C)-Tb(1)-O(2) | 133.44(11) | O(2W)-Tb(1)-O(2) | 143.34(11) |
| O(3W)-Tb(1)-O(2) | 75.05(12) | O(1W)-Tb(1)-O(2) | 122.97(11) |
| O(3A)-Tb(1)-O(5C) | 121.09(10) | O(4B)-Tb(1)-O(5C) | 143.52(10) |
| O(1)-Tb(1)-O(5C) | 69.58(10) | O(6C)-Tb(1)-O(5C) | 52.06(9) |
| O(2W)-Tb(1)-O(5C) | 71.76(10) | O(3W)-Tb(1)-O(5C) | 72.28(10) |
| O(1W)-Tb(1)-O(5C) | 118.30(10) | O(2)-Tb(1)-O(5C) | 117.28(10) |

Symmetry code A: *x*, 0.5-*y*, 0.5+*z*; B: -*x*, -0.5+*y*, 2.5-*z*; C: 1-x, -0.5+y, 1.5-z.

**Table S2** Selective bond distance (Å) and angle (°) in Nd−**MDIA.**

| | | | |
|---|---|---|---|
| Nd(1)-O(8A) | 2.340(5) | Nd(1)-O(7B) | 2.372(5) |
| Nd(1)-O(1C) | 2.488(5) | Nd(1)-O(1W) | 2.532(5) |
| Nd(1)-O(3W) | 2.538(6) | Nd(1)-O(2W) | 2.543(5) |
| Nd(1)-O(4) | 2.555(5) | Nd(1)-O(2C) | 2.593(5) |
| Nd(1)-O(3) | 2.599(5) | | |
| O(8A)-Nd(1)-O(7B) | 100.1(2) | O(8A)-Nd(1)-O(1C) | 76.8(2) |
| O(7B)-Nd(1)-O(1C) | 142.6(2) | O(8A)-Nd(1)-O(1W) | 145.4(2) |
| O(7B)-Nd(1)-O(1W) | 81.8(2) | O(1C)-Nd(1)-O(1W) | 81.2(2) |
| O(8A)-Nd(1)-O(3W) | 145.0(2) | O(7B)-Nd(1)-O(3W) | 76.1(2) |
| O(1C)-Nd(1)-O(3W) | 127.0(2) | O(1W)-Nd(1)-O(3W) | 69.3(2) |
| O(8A)-Nd(1)-O(2W) | 76.3(2) | O(7B)-Nd(1)-O(2W) | 72.3(2) |
| O(1C)-Nd(1)-O(2W) | 70.7(2) | O(1W)-Nd(1)-O(2W) | 71.3(2) |
| O(3W)-Nd(1)-O(2W) | 132.1(2) | O(8A) Nd(1)-O(4) | 72.4(2) |
| O(7B)-Nd(1)-O(4) | 69.32(18) | O(1C)-Nd(1)-O(4) | 139.7(2) |
| O(1W)-Nd(1)-O(4) | 137.6(2) | O(3W)-Nd(1)-O(4) | 73.9(2) |
| O(2W)-Nd(1)-O(4) | 124.17(18) | O(8A)-Nd(1)-O(2C) | 109.79(19) |
| O(7B)-Nd(1)-O(2C) | 150.12(19) | O(1C)-Nd(1)-O(2C) | 51.03(17) |
| O(1W)-Nd(1)-O(2C) | 74.57(19) | O(3W)-Nd(1)-O(2C) | 78.6(2) |
| O(2W)-Nd(1)-O(2C) | 115.56(18) | O(4)-Nd(1)-O(2C) | 118.07(16) |
| O(8A)-Nd(1)-O(3) | 78.2(2) | O(7B)-Nd(1)-O(3) | 117.25(18) |
| O(1C)-Nd(1)-O(3) | 98.83(19) | O(1W)-Nd(1)-O(3) | 131.91(18) |
| O(3W)-Nd(1)-O(3) | 73.3(2) | O(2W)-Nd(1)-O(3) | 154.1(2) |
| O(4)-Nd(1)-O(3) | 50.13(15) | O(2C)-Nd(1)-O(3) | 69.23(16) |

Symmetry code A: *x*, -1+*y*, *z*; B: 1-*x*, 2-*y*, 1-*z*; C: 1+x, y, z.

**Table S3** Selective bond distance (Å) and angle (°) in Ho−**MDIA.**

| | | | |
|---|---|---|---|
| Ho(1)-O(5A) | 2.261(3) | Ho(1)-O(6B) | 2.296(3) |
| Ho(1)-O(3) | 2.326(3) | Ho(1)-O(3W) | 2.354(3) |
| Ho(1)-O(1W) | 2.363(3) | Ho(1)-O(8C) | 2.387(3) |
| Ho(1)-O(7C) | 2.455(3) | Ho(1)-O(2W) | 2.469(3) |
| O(5A)-Ho(1)-O(6B) | 96.81(10) | O(5A)-Ho(1)-O(3) | 94.99(11) |
| O(6B)-Ho(1)-O(3) | 140.28(10) | O(5A)-Ho(1)-O(3W) | 153.71(13) |
| O(6B)-Ho(1)-O(3W) | 72.95(11) | O(3)-Ho(1)-O(3W) | 79.86(11) |
| O(5A)-Ho(1)-O(1W) | 77.77(12) | O(6B)-Ho(1)-O(1W) | 70.60(10) |
| O(3)-Ho(1)-O(1W) | 149.12(11) | O(3W)-Ho(1)-O(1W) | 119.11(12) |
| O(5A)-Ho(1)-O(8C) | 78.18(10) | O(6B)-Ho(1)-O(8C) | 144.24(10) |
| O(3)-Ho(1)-O(8C) | 75.38(10) | O(3W)-Ho(1)-O(8C) | 124.26(10) |
| O(1W)-Ho(1)-O(8C) | 73.76(10) | O(5A)-Ho(1)-O(7C) | 130.67(10) |
| O(6B)-Ho(1)-O(7C) | 114.88(10) | O(3)-Ho(1)-O(7C) | 84.18(11) |
| O(3W)-Ho(1)-O(7C) | 74.82(11) | O(8C)-Ho(1)-O(7C) | 53.79(9) |
| O(5A)-Ho(1)-O(2W) | 75.39(11) | O(6B)-Ho(1)-O(2W) | 74.36(10) |
| O(3)-Ho(1)-O(2W) | 72.22(10) | O(3W)-Ho(1)-O(2W) | 78.51(11) |
| O(1W)-Ho(1)-O(2W) | 132.34(11) | O(8C)-Ho(1)-O(2W) | 135.66(10) |
| O(7C)-Ho(1)-O(2W) | 147.01(10) | | |

Symmetry code A: 2-*x*, 1-*y*, 2-*z*; B: -1+*x*, *y*, *z*; C: 2-x, 0.5+y, 1.5-z.

**Figure S8** TGA traces of Tb−**MDIA** ranging from room temperature to 500 °C.

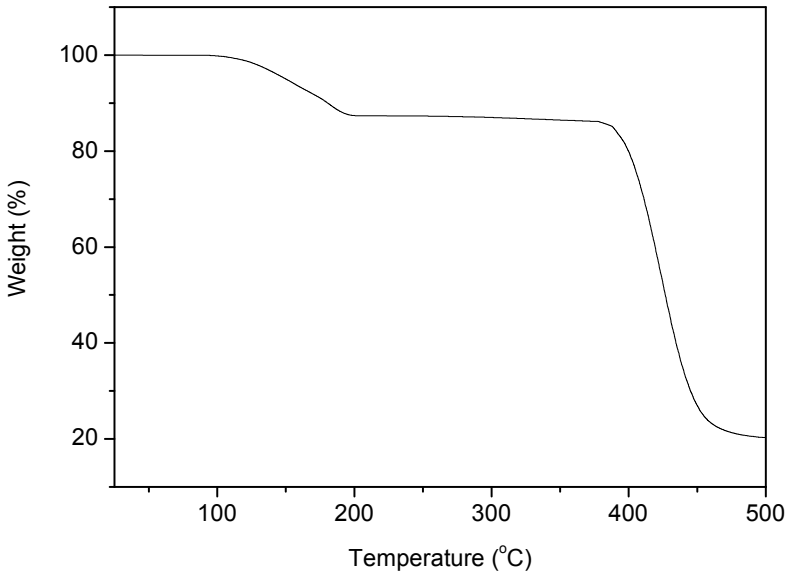


**Figure S9** The Stern−Volmer plot of Tb−**MDIA** quenched by $Fe^{3+}$, where $I_0$ and I are the fluorescence intensity before and after $Fe^{3+}$ incorporation, respectively.

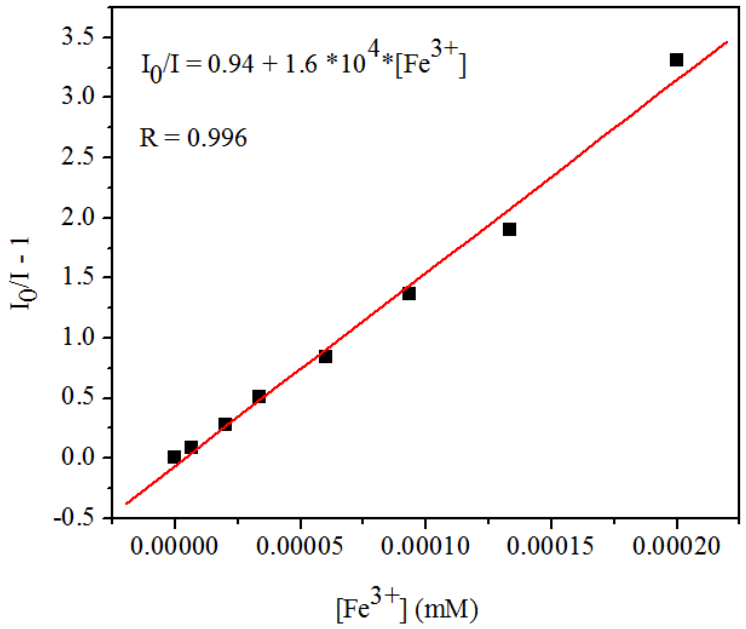

**Figure S10** Families of various fluorescence spectra of Tb−**MDIA** (0.33 g/L) in water solution upon the addition of 0.4 mM of different selected analytes.

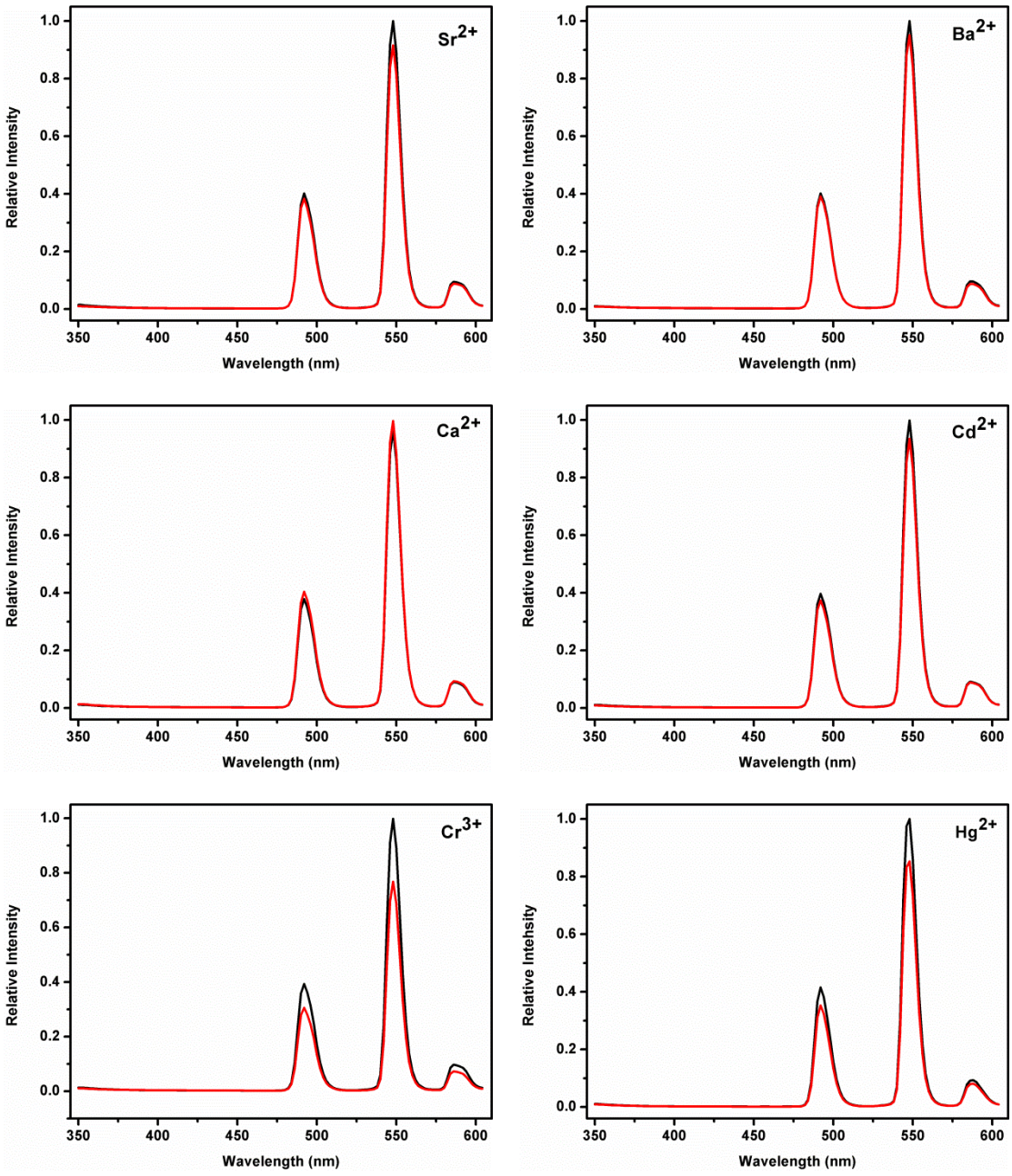

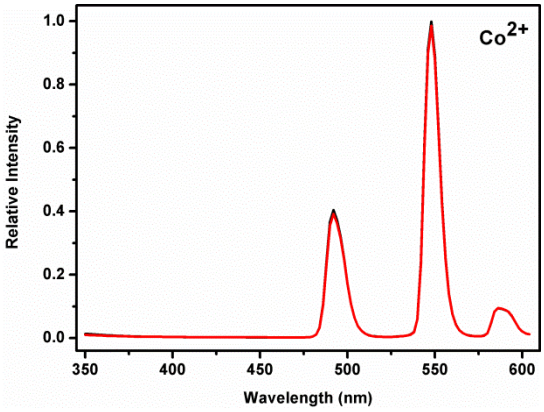
Co2+
Relative Intensity
Wavelength (nm)

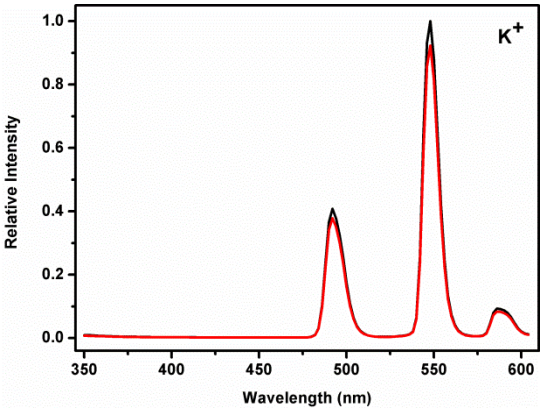
K+
Relative Intensity
Wavelength (nm)

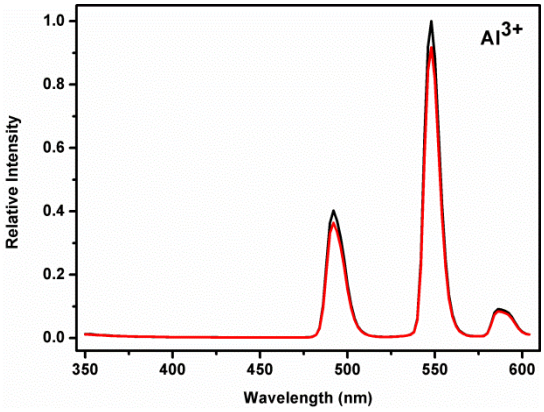
Al3+
Relative Intensity
Wavelength (nm)

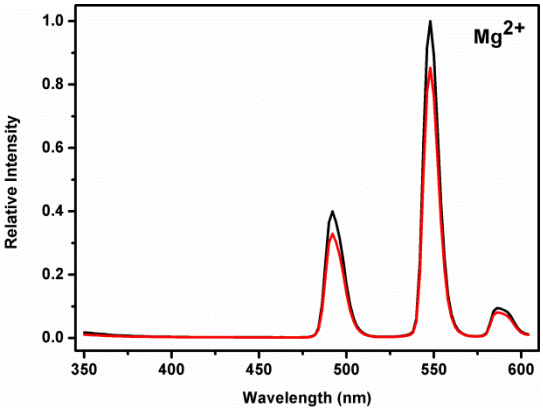
Mg2+
Relative Intensity
Wavelength (nm)

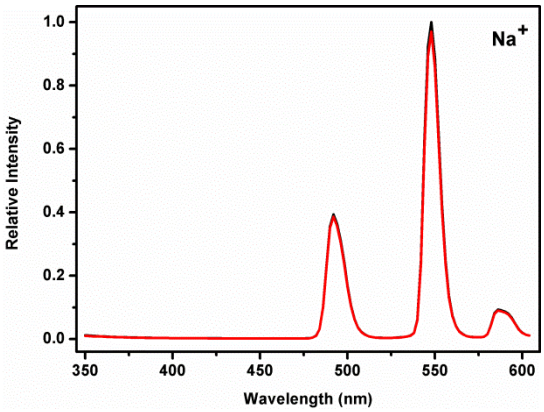
Na+
Relative Intensity
Wavelength (nm)

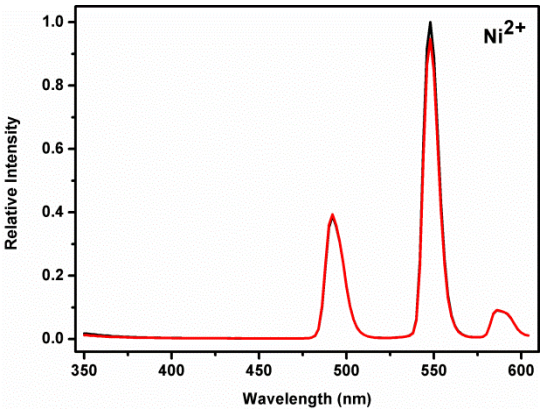
Ni2+
Relative Intensity
Wavelength (nm)

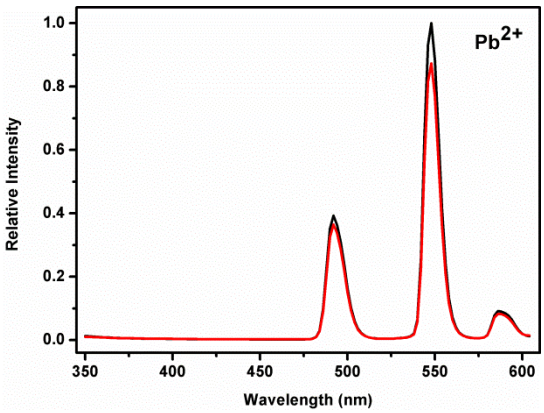
Pb2+
Relative Intensity
Wavelength (nm)

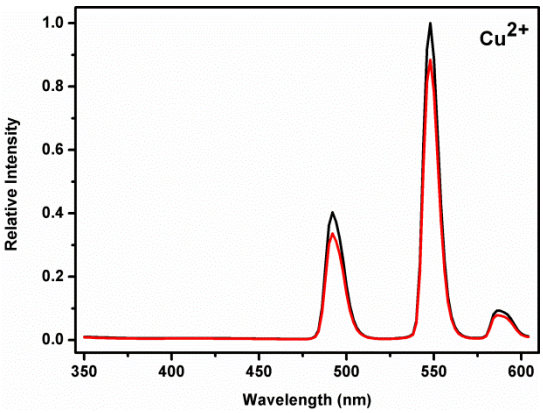
Cu2+
Relative Intensity
Wavelength (nm)

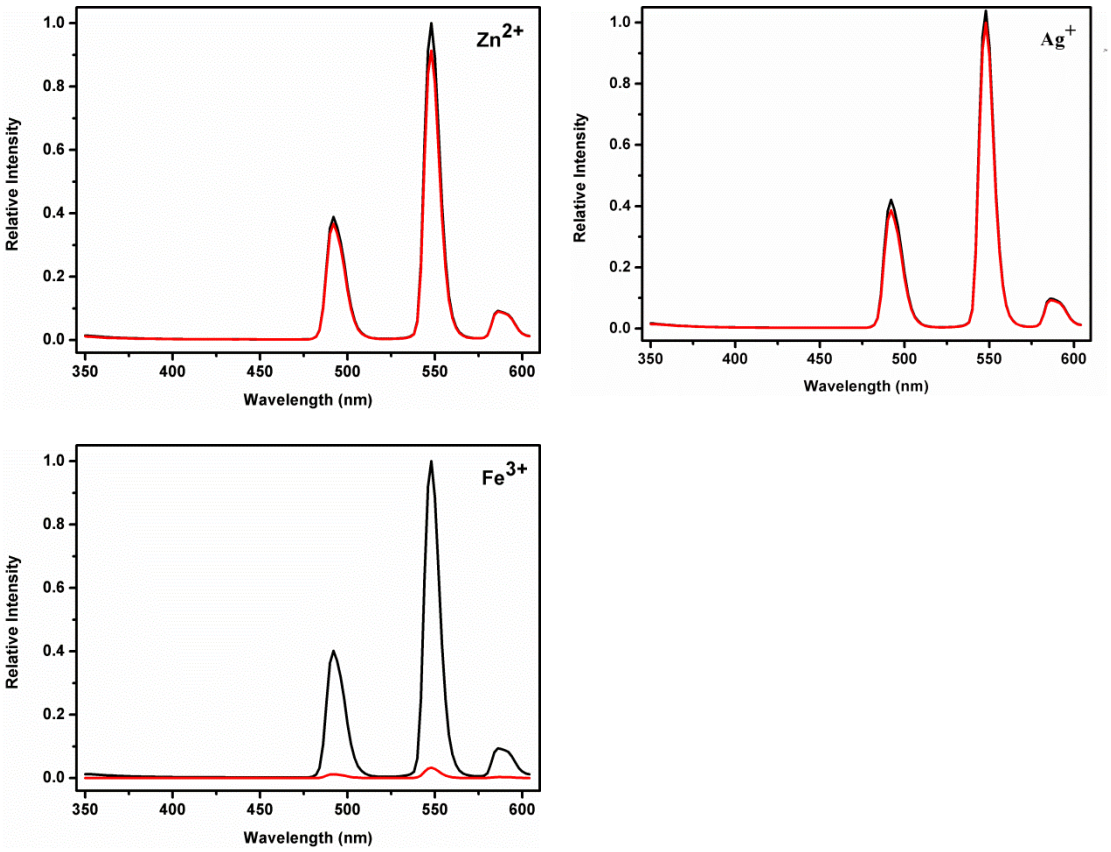


**Figure S11** Fluorescence spectra of Tb−**MDIA** (0.33 g/L) with gradual addition of different concentrations of $Fe^{3+}$ ions in HEPES aqueous solutions.

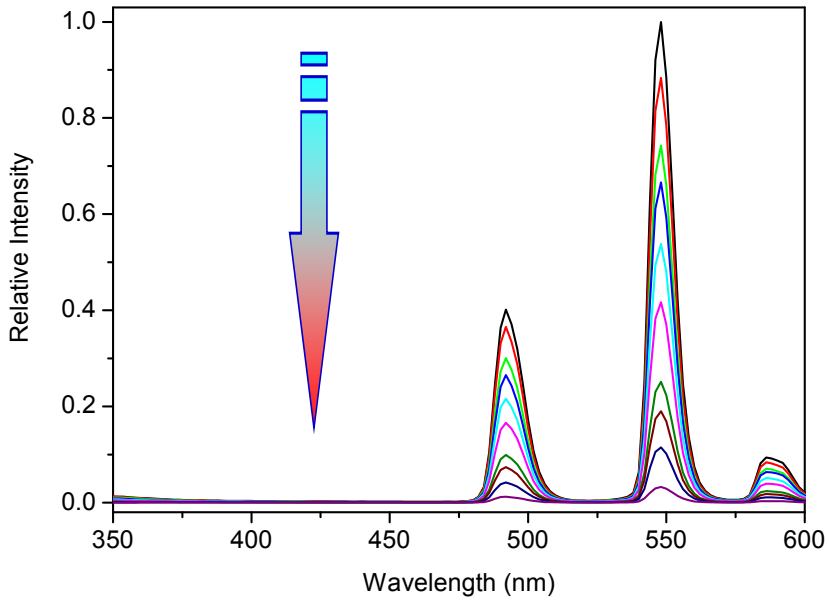

**Figure S12** The Stern−Volmer plot of Tb−**MDIA** quenched by PA ethanol solution, where $I_0$ and I are the fluorescence intensity before and after PA incorporation, respectively.

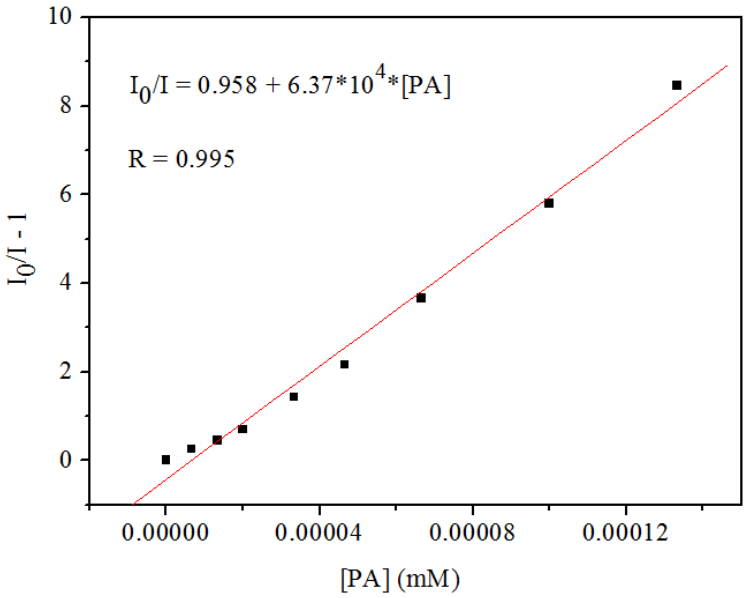


**Figure S13** Powder X-ray diffraction (XRD) profiles for as-synthesized Tb−**MDIA** and Tb−**MDIA** samples after the PA detection.

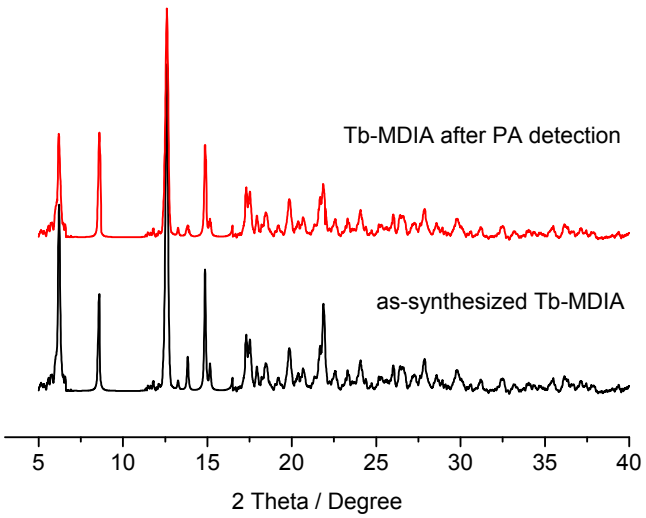

**Figure S14** Families of various fluorescence spectra of Tb−**MDIA** (0.33 g/L) in ethanol solution upon the addition of 0.33 mM of different selected analytes.

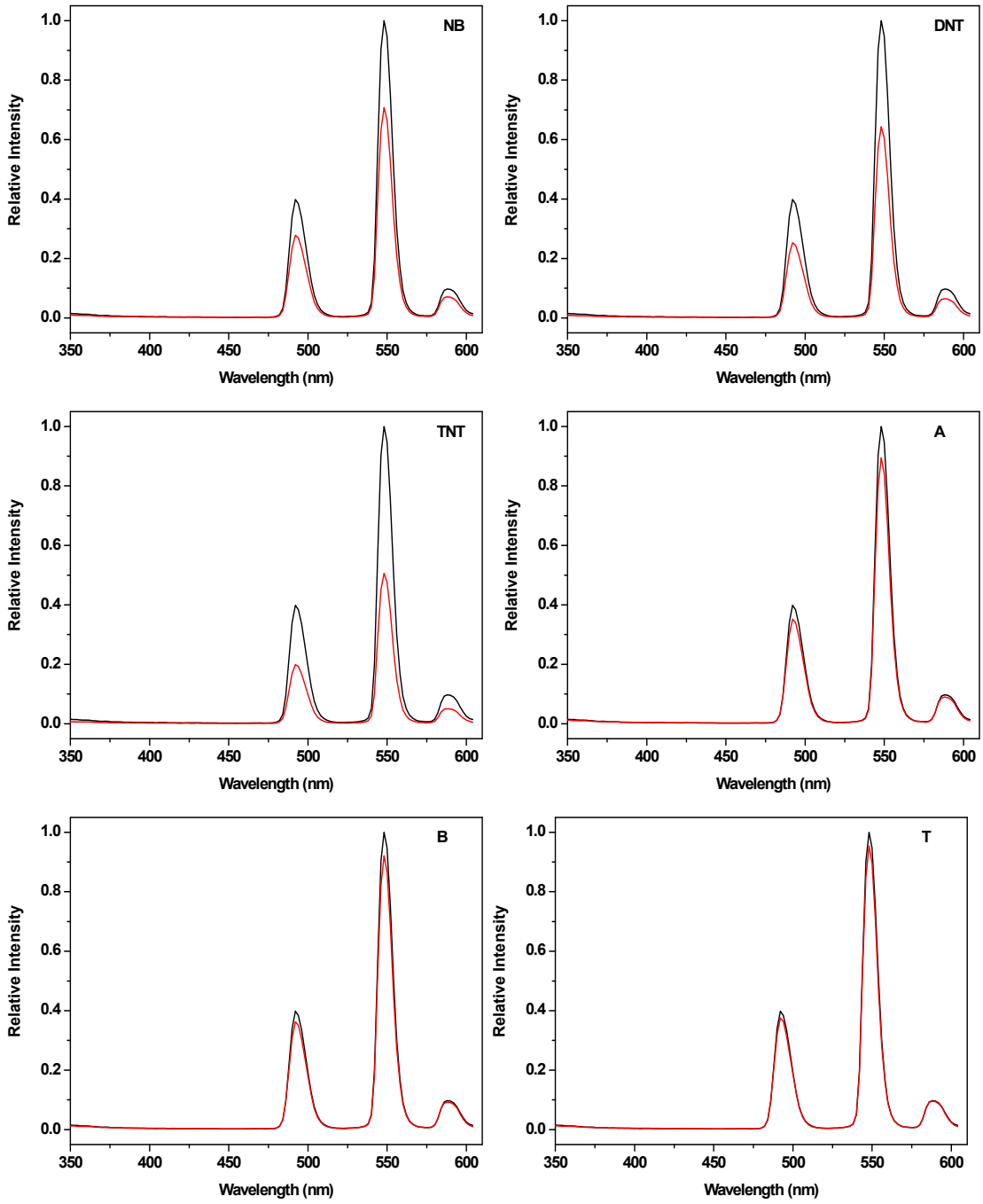

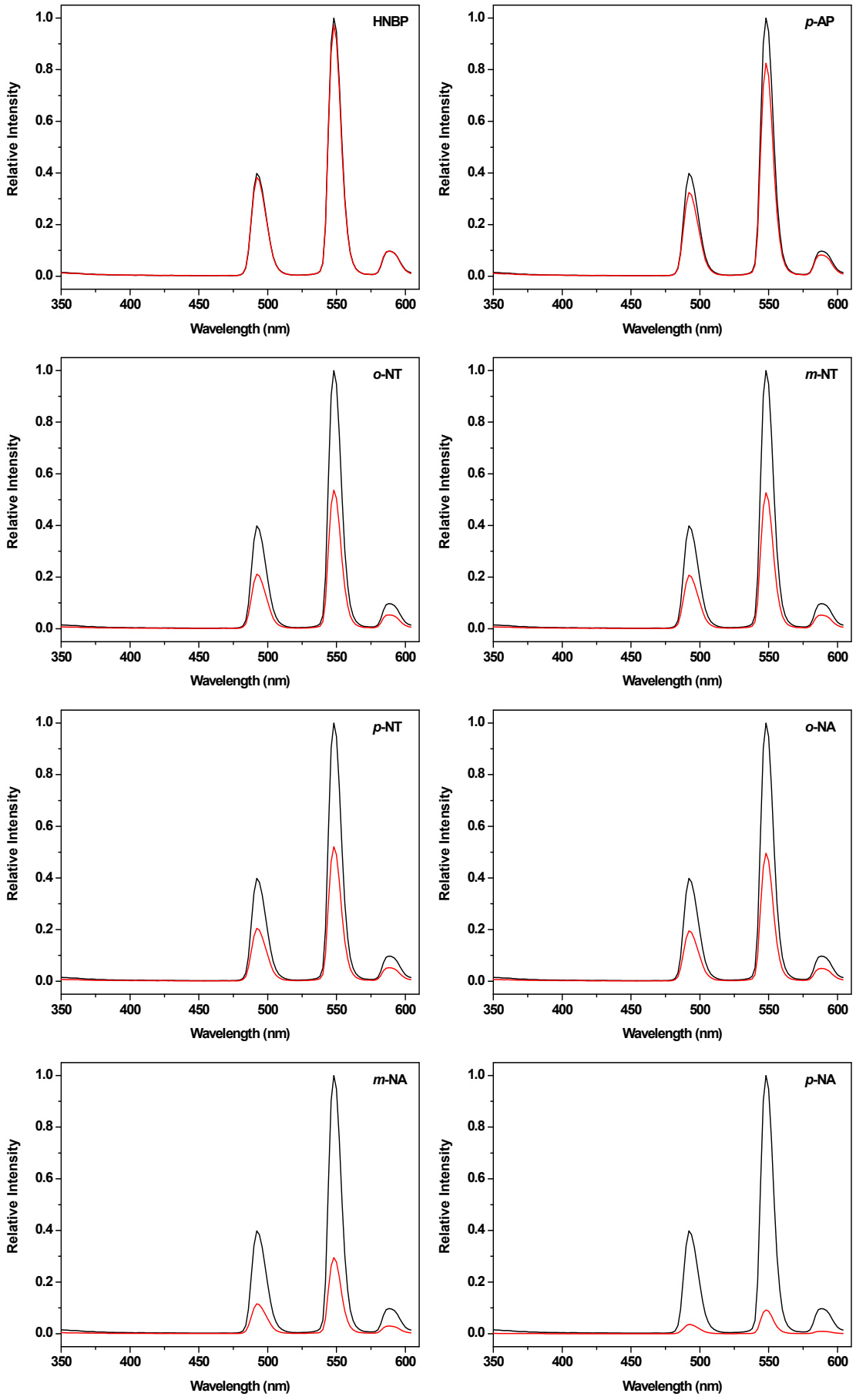
HNBP
p-AP
o-NT
m-NT
p-NT
o-NA
m-NA
p-NA
Relative Intensity
Wavelength (nm)
0.0
0.2
0.4
0.6
0.8
1.0
350
400
450
500
550
600

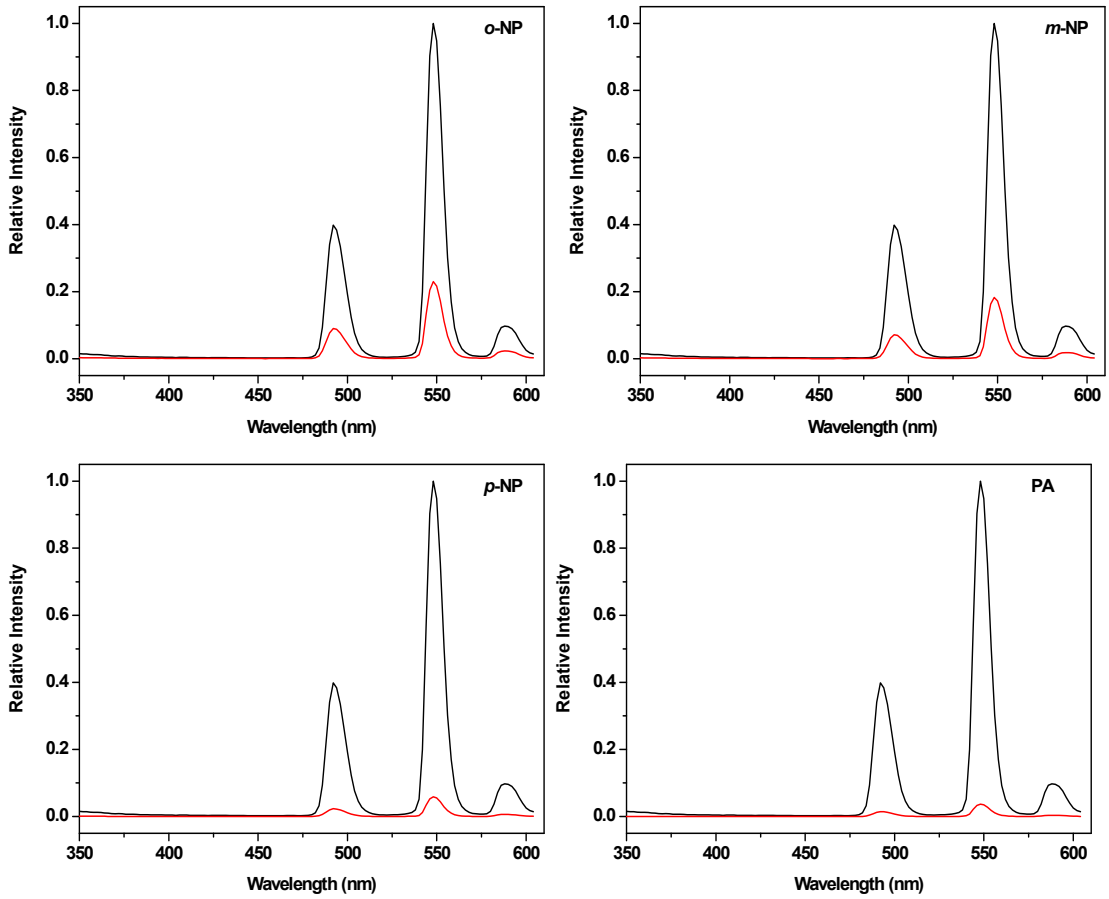
o-NP
m-NP
p-NP
PA
Relative Intensity
Wavelength (nm)
0.0
0.2
0.4
0.6
0.8
1.0
350
400
450
500
550
600

**Figure S15** Yields of 2-phenyl-2-((trimethylsilyl)oxy)acetonitrile catalyzed by Ho−**MDIA** (violet) and without Ho−**MDIA** through filtration after 2 h of the reaction (green).

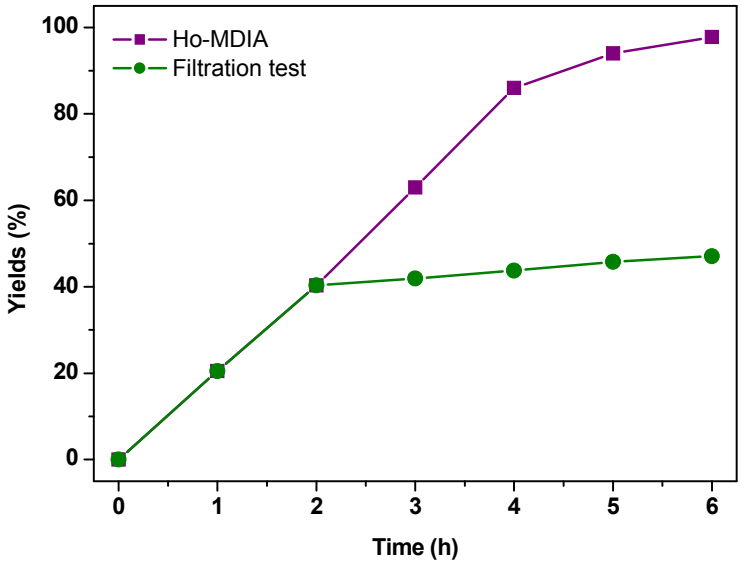


**Figure S16** Study on recycling of catalyst Ho−**MDIA** for the heterogeneous cyanosilylation: $(CH_3)_3SiCN$: 1.2 mmol; benzaldehyde: 0.5 mmol; Ho−**MDIA** catalysts: 2 mol%, room temperature for 6 hours.

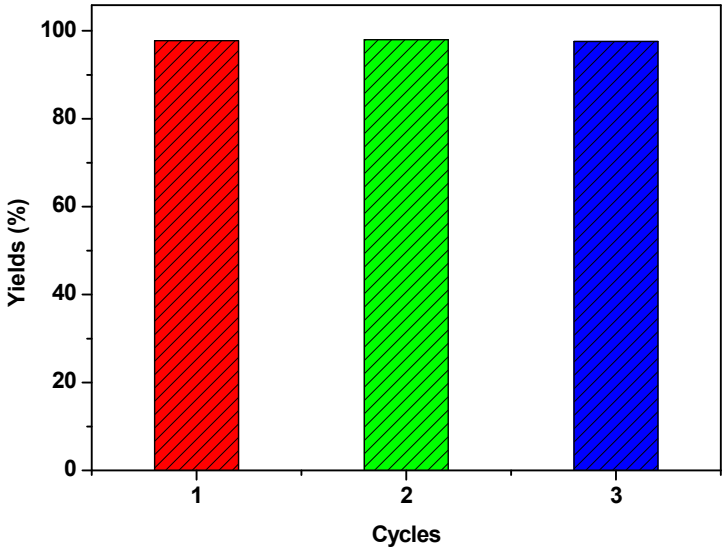

**Figure S17** Powder X-ray diffraction (XRD) profiles for as-synthesized Ho−**MDIA**/Nd−**MDIA** and Ho−**MDIA**/Nd−**MDIA** samples after the third catalytic cycles.

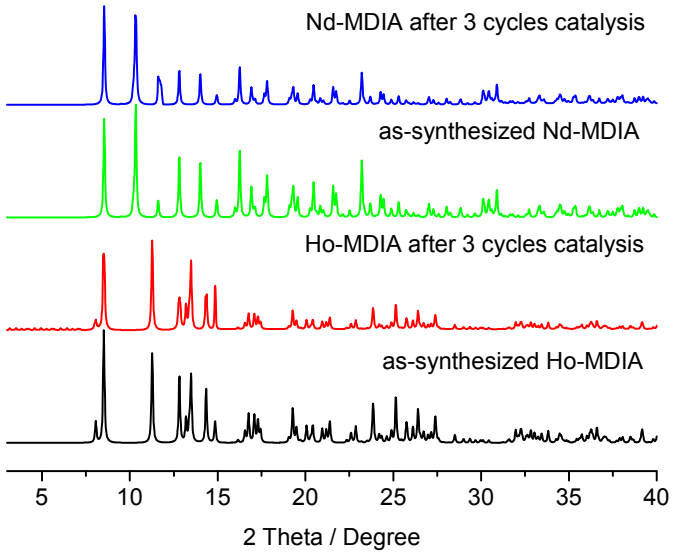

**Table S4** Comparison with different MOF catalysts in the catalysis of cyanosilylation reaction of benzaldehyde with $(CH_3)_3SiCN$.

| Entry | Catalyst | T (℃) | t (hr) | Yield(%) | Ref. |
|---|---|---|---|---|---|
| **1** | 1·Cd | r.t. | 18 | 94 | [S1] |
| **2** | Cd-PBA | r.t. | 8 | 99 | [S2] |
| **3** | Ce-MDIP1 | r.t. | 24 | 93 | [S3] |
| **4** | Ce-MDIP2 | r.t. | 24 | 94 | [S3] |
| **5** | Eu-PDC | r.t. | 3 | 93 | [S4] |
| **6** | MIL-47 (V) | r.t. | 3 | 46 | [S5] |
| **7** | MIL-53 (Al) | r.t. | 3 | 26 | [S5] |
| **8** | MIL-101 (Cr) | r.t. | 4 | 96 | [S5] |
| **9** | Zn-MOF | r.t. | 10 | 74 | [S6] |
| **10** | Ce-MOF | r.t. | 2 | 94 | [S7] |
| **11** | Ps-CMOF | r.t. | 48 | 93 | [S8] |
| **12** | POMOF-1 | r.t. | 24 | 98 | [S9] |
| **13** | UPC-15 | r.t. | 24 | 99 | [S10] |
| **14** | UPC-16 | r.t. | 24 | 97 | [S10] |
| **15** | Co-MOF | r.t. | 12 | 98 | [S11] |
| **16** | Cd-bpdc | r.t. | 14 | 95 | [S12] |
| **17** | Mn-MOF | r.t. | 9 | 98 | [S13] |
| **18** | Ho–MDIA | r.t. | 6 | 97.8 | This work |

**Reference**

S1. Jiang, W.; Yang, J.; Liu, Y.-Y.; Song, S.-Y.; Ma, J.-F. A stable porphyrin-based porous mog metal–organic framework as an efficient solvent-free catalyst for C–C bond formation. *Inorg. Chem.* **2017**, *56*, 3036-3043.

S2. Hu, L.; Hao, G.-X.; Luo, H.-D.; Ke, C.-X.; Shi, G.; Lin, J.; Lin, X.-M.; Qazi, U. Y.; Cai, Y.-P. Bifunctional 2D Cd(II)-based metal–organic framework as efficient heterogeneous catalyst for the formation of C–C bond. *Cryst. Growth Des.* **2018**, *5*, 2883-2889.

S3. Dang, D.; Wu, P.; He, C.; Xie, Z.; Duan, C. Homochiral metal−organic frameworks for heterogeneous asymmetric catalysis. *J. Am. Chem. Soc.* **2010**, *132*, 14321-14323.

S4. Lin, X.-M.; Niu, J.-L.; Wen, P.-X.; Pang, Y.; Hu, L.; Cai, Y.-P. A polyhedral metal–organic framework based on supramolecular building blocks: catalysis and luminescent sensing of solvent molecules. *Cryst. Growth Des.* **2016**, *16*, 4705-4710.

S5. Zhang, Z.; Chen, J.; Bao, Z.; Chang, G.; Xing, H.; Ren, Q. Insight into the catalytic properties and applications of metal–organic frameworks in the cyanosilylation of aldehydes. *RSC Adv.* **2015**, *5*, 79355-79360.

S6. Karmakar, A.; Paul, A.; Rúbio, G. M. D. M.; da Silva, M. F. C. G.; Pombeiro, A. J. L. Zinc(II) and Copper(II) metal-organic frameworks constructed from a terphenyl-4,4″-dicarboxylic acid derivative: synthesis, structure, and catalytic application in the cyanosilylation of aldehydes. *Eur. J. Inorg. Chem.* **2016**, *2016*, 5557-5567.

S7. Karmakar, A.; Rubio, G. M. D. M.; Paul, A.; da Silva, M. F. C. G.; Mahmudov, K. T.; Guseinov, F. I.; Carabineiro, S. A. C.; Pombeiro, A. J. L. Lanthanide metal organic frameworks based on dicarboxyl-functionalized arylhydrazone of barbituric

acid: syntheses, structures, luminescence and catalytic cyanosilylation of aldehydes. *Dalton Trans.* **2017**, *46*, 8649-8657.

S8. Li, J.; Ren, Y.; Qi, C.; Jiang, H. The first porphyrin–salen based chiral metal–organic framework for asymmetric cyanosilylation of aldehydes. *Chem. Commun.* **2017**, *53*, 8223-8226.

S 9. Han, Q.; Sun, X.; Li, J.; Ma, P.; Niu, J. Novel isopolyoxotungstate $[H_2W_{11}O_{38}]^{8-}$ based metal organic framework: as Lewis acid catalyst for cyanosilylation of aromatic aldehydes. *Inorg. Chem.* **2014**, *53*, 6107-6112.

S10. Wang, X.; Zhang, L.; Yang, J.; Dai, F.; Wang, R.; Sun, D. Metal-ion metathesis and properties of triarylboron-functionalized metal-organic frameworks. *Chem. Asian J.* **2015**, *10*, 1535-1540.

S11. Cui, X.; Xu, M.-C.; Zhang, L.-J.; Yao, R.-X.; Zhang, X.-M. Solvent-free heterogeneous catalysis for cyanosilylation in a dynamic cobalt-MOF. *Dalton Trans.* **2015**, *44*, 12711-12716.

S12. Bhunia, A.; Dey, S.; Moreno, J. M.; Diaz, U.; Concepcion, P.; Van Hecke, K.; Janiak, C.; Van Der Voort, P. A homochiral vanadium–salen based cadmium bpdc MOF with permanent porosity as an asymmetric catalyst in solvent-free cyanosilylation. *Chem. Commun.* **2016**, *52*, 1401-1404.

S13. Horike, S.; Dincă, M.; Tamaki, K.; Long, J. R. Size-selective Lewis acid catalysis in a microporous metal-organic framework with exposed $Mn^{2+}$ coordination sites. *J. Am. Chem. Soc.* **2008**, *130*, 5854-5855.